Draft version February 22, 2019
Typeset using LaTeX **twocolumn** style in AASTeX62

Enhanced chromospheric 3-minute oscillatory power associated with the 2011-February-15 X2.2 flare

Laurel Farris[1] and R. T. James McAteer[1]

[1] *New Mexico State University*

ABSTRACT

The origin of the 3-minute oscillations of the chromosphere has been attributed to both slow magnetoacoustic waves propagating from the photosphere, and to oscillations generated within the chromosphere itself at its natural frequency as a response to a disturbance. Here we present an investigation of the spatial and temporal behavior of the chromospheric 3-minute oscillations before, during, and after the SOL2011-02-15T01:56 X2.2 flare. Ultraviolet emission at 1600 and 1700 Angstroms obtained at 24-second cadence from the Atmospheric Imaging Assembly on board the Solar Dynamics Observatory was used to create power maps as functions of both space and time. A Fourier transform was applied to the intensity signal from individual pixels starting at each observation time over time segments 64 frames (25.6 minutes) in length. We detect an increase in the 3-minute power during the X-class flare, as well as during other smaller events before and after the flare. The enhancement is concentrated in small areas, supporting the injection of energy by nonthermal particles. The potential correlation between 3-minute power and magnetic field strength is discussed, along with formation height dependencies.

Keywords: chromosphere, flares, oscillations

1. INTRODUCTION

Most of the radiative energy associated with solar flares is emitted from the chromosphere in the form of optical and UV emission, but the mechanism of energy transport from the magnetic reconnection site to the chromosphere and subsequent conversion to other forms remains unclear. The chromosphere has been observed to oscillate in response to an injection of energy, suggesting that the nature of such oscillations may reveal something about the nature of energy deposition and conversion associated with flares. In this paper, we aim to characterize the oscillatory response of the chromosphere before, during, and after an X-class flare with the goal of further investigating the "flaring chromosphere" and helping to constrain the origin of the persistent 3-minute oscillations in the chromosphere.

The 3-minute oscillations observed in the chromosphere have been attributed to the upward propagation of slow magnetoacoustic waves that originate in deeper layers of the solar atmosphere. The acoustic cutoff frequency at the base of the chromosphere, $\nu_0 \approx 5.6$ mHz ($\sim$3 minute period), effectively creates a barrier across which waves can travel only if their propagation frequency is higher than ν_0. Another explanation is that the acoustic cutoff frequency is the natural frequency at which the chromospheric plasma will respond to a disturbance. This was predicted and shown numerically by a series of papers by Sutmann & Ulmschneider (1995a,b); Sutmann et al. (1998), and other studies by Chae & Goode (2015). Enhancement of oscillations close to a period of 3 minutes has since been observed associated with a variety of phenomenae. Kwak et al. (2016) observed the response of the chromosphere to a downflow event using high-resolution spectra from the *Interface Region Imaging Spectrograph* (*IRIS*; De Pontieu et al. (2014)). **?** detected a different type of oscillations above an active region associated with a flare.

Milligan et al. (2017) observed an enhancement in the 3-minute power from thermal emission that was not present in X-ray emission associated with the flare. supporting the prediction that the chromosphere naturally responds to an impulsive disturbance at the acoustic cutoff frequency.

Kumar & Ravindra (2006) observed an enhancement in velocity oscillations between 5 and 6.5 mHz in emission in close proximity to the source of HXR emission in RHESSI images, and interpreted this locally concentrated enhancement as energy injection by non-thermal particles.

Brosius & Daw (2015) studied UV stare spectra of an M-class flare in Si IV, C I, and O IV lines, and reported four complete intensity fluctuations with periods around 171 seconds, in furthor support of the model of energy injection in the chromosphere by non-thermal particle beams.

The 3-minute period falls within the typical range of periods observed in the form of small-scale fluctuations known as quasi-periodic pulsations (QPPs). QPPs have been observed in flare emission throughout all stages and across all wavelength bands, and are considered to be intrinsic signatures of flare dynamics. In particu-

lar, QPPs in thermal emission from the chromosphere may provide a tool for investigating the transportation of energy from the flare site down into the chromosphere (Inglis et al. 2015).

Sych et al. (2009) suggested that the leakage of umbral 3-minute oscillations into the upper atmosphere was the cause of flaring QPPs, supported by observations of a similar periodicity in the flare emission.

Monsue et al. (2016) observed an enhancement of frequencies between 1 and 8 mHz associated with an M- and X-class flare in Hα emission integrated over the AR, but investigation of subregions revealed an enhancement at low frequencies (1-2 mHz) in inner flare regions before and after the flare, and a suppression of oscillatory power over all frequencies between 1 and 8 mHz during the main phases.

Awasthi et al. (2018) found two distinct pre-flare phases, beginning with non-thermal particles and evolving into a thermal conduction front. Fletcher et al. (2013) studied both the thermal and non-thermal response of the chromosphere during the early stages of an M-class flare, and found the main flux to originate from a different location from the initial brightenings.

The goal of the present study is to investigate the location of power enhancement before, during, and after a flare. The extra time will allow comparison between flaring and non-flaring chromosphere to distinguish whether the plasma is oscillating at the natural frequency of the chromosphere or responding to an impulsive injection of energy. The location of power enhancement will help probe the nature of the energy deposition at various phases.

Here we present the spatial and temporal evolution of 3-minute power in the chromosphere during the *GOES* X-class flare that occurred on 15 February 2011. The Atmospheric Imaging Assembly (AIA; Lemen et al. (2012)) on board the *Solar Dynamics Observatory* (SDO; Pesnell et al. (2012)) provides images with a spatial size scale of 0.6" per pixel and 24-second cadence in thermal UV emssion from two channels that sample the lower atmosphere. These data allow the computation of spatially resolved power maps centered on the frequency of interest. The flare, data, and methodology are described in §2. Results are presented and discussed in §4. We conclude in §5 with key preliminary findings and plans for the continuation and development of this work.

2. OBSERVATIONS AND DATA REDUCTION

The 2011 February 15 X2.2 flare occurred in NOAA active region (AR) 11158 close to disk center during solar cycle 24 (SOL2011-02-15T01:56). The AR was composed of a quadrupole: two sunspot pairs (four sunspots total). The X-flare occurred in a delta-spot composed of the leading spot of the southern pair and the trailing spot of the northern pair. It started at 01:44UT, peaked at 01:56UT, and ended at 02:06UT, as determined by the soft X-ray flux from the *Geostationary Operational Environmental Satellite* (*GOES*-15; Viereck et al. (2007)). The impulsive phase lasted about 10 minutes. Data covering 5 hours centered on this flare were used for the analysis. This data includes a C-class flare that occurred between 00:30 and 00:45 UT on 15 February 2011.

SDO/AIA obtains full disk images throughout the solar atmosphere, using narrow band filters centered on 10 different wavelengths, two of which provide measurements of thermal UV emission from the chromosphere . The 1700Å channel mostly contains continuum emission from the temperature minimum, and the 1600Å channel covers both continuum emission and the C IV spectral line in the upper photosphere and transition region. Both channels have a cadence of 24 seconds and spatial size scale of 0.6 arcseconds per pixel.

Data from the Helioseismic and Magnetic Imager (HMI; Scherrer et al. (2012)), also on board *SDO*, is used to study potential correlations between magnetic field strength and oscillatory behavior in the chromosphere. HMI obtains full disk data in the form of line-of-sight magnetograms, vector magnetograms, Doppler velocity, and continuum intensity, measured at the Fe I absorption line at 6173Å with a passband width of 0.076Å. Each data product has a cadence of 45 seconds (with the exception of the vector magnetograms, at 135 seconds), and spatial size scale of 0.5 arcseconds per pixel (Schou et al. 2012).

The standard data reduction routine *aia_prep.pro* from solarsoft was applied to all data .

Figure 1 shows light curves for the full 5-hour time series from 00:00 to 04:59 on 2011-February-15. The top panel shows both AIA channels. The bottom panel shows both SXR channels from *GOES-15* at 1-8Å (black curve) and 0.5-4Å (pink curve). A small C-flare occurred before the X-flare between 00:30 and 00:45 UT, and two small events occurred after the X-flare, between 03:00 and 03:15, and between 04:25 and 04:45.

Pre-flare images of the full disk are shown in Figure 2, along with a 300x198 arcsecond subset of the data centered on AR 11158. This subset was extracted and aligned by cross correlation (McAteer et al. 2003, 2004). Images were scaled to improve contrast using the *aia_intscale.pro* routine from *sswidl*. The magnetic configuration of the quadrupole is clear in the HMI magnetograms. The northern pair will be designated as AR_1 and the southern pair will be designated as AR_2. Sunspots in the northern pair will be designated as AR_1a (positive polarity) and AR_1b (negative polarity). Sunspots in the southern pair will be designated as AR_2a (positive polarity) and AR_2b (negative polarity).

Both AIA channels saturated ($\geq$15000 counts) in the center during the peak of the X-class flare, and a few pixels also saturated during the smaller events before and after. Affected pixels were all contained within the 300x198 arcsecond subset of data throughout the duration of the time series. Four images from the 1700Å channel on AIA were missing, between the images with start times at 00:59:53.12, 01:59:29.12, 02:59:05.12, and 03:58:41.12, and the following images, each with start times 48 seconds after the previous image. Since the gaps in data were separated by an hour, it was reasonable to approximate missing images by averaging the two adjacent images.

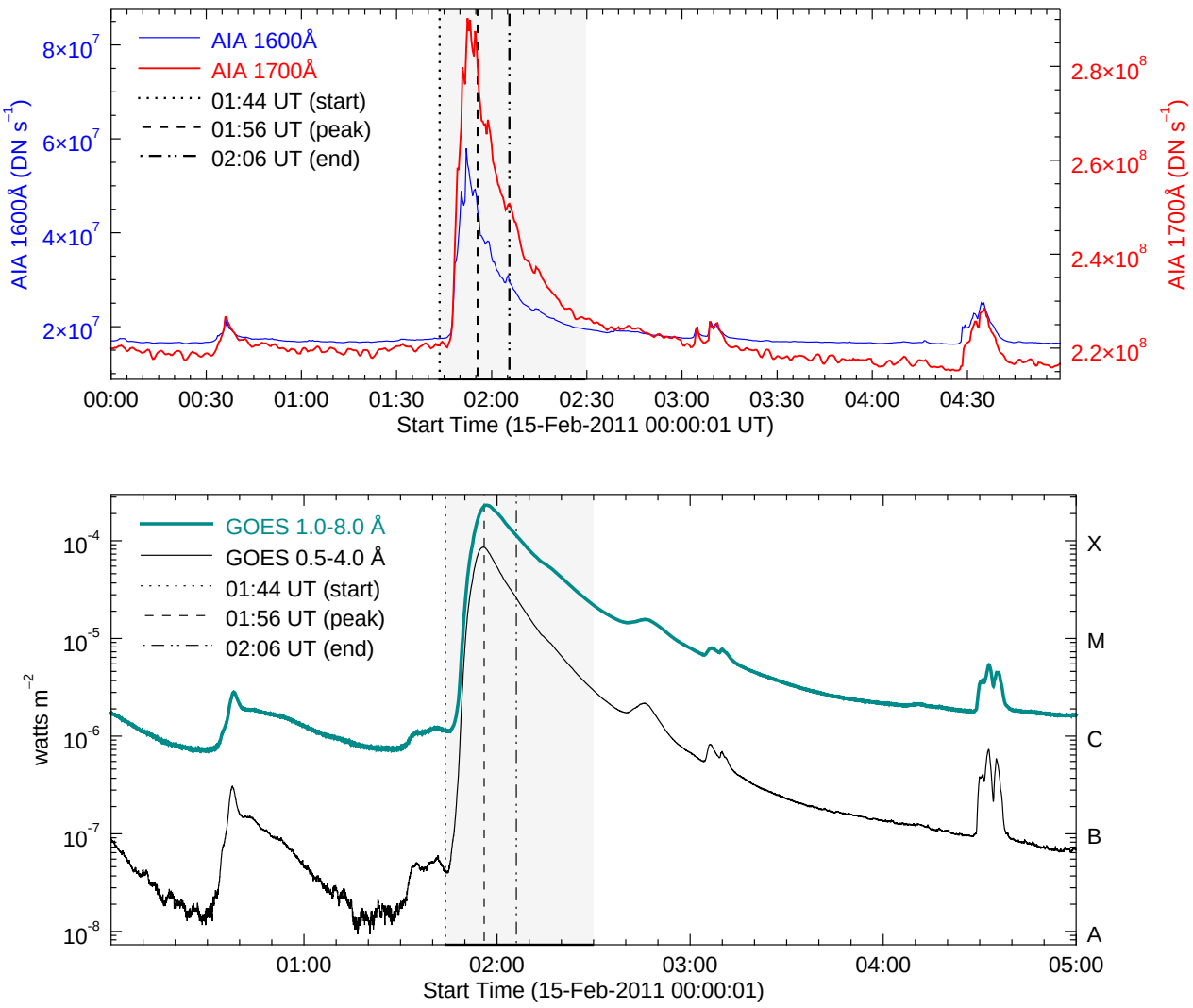

Fig. 1. Top: Light curves of the UV continuum emission from AIA 1600Å (blue curve) and AIA 1700Å (red curve), integrated over the flare region in AR 11158. Bottom: Light curves observed by the *GOES-15* satellite channels 1-8Å (black curve) and 0.5-4Å (pink curve), scaled as log(flux) to enable visibility of the increases during smaller events before and after the main X-flare.

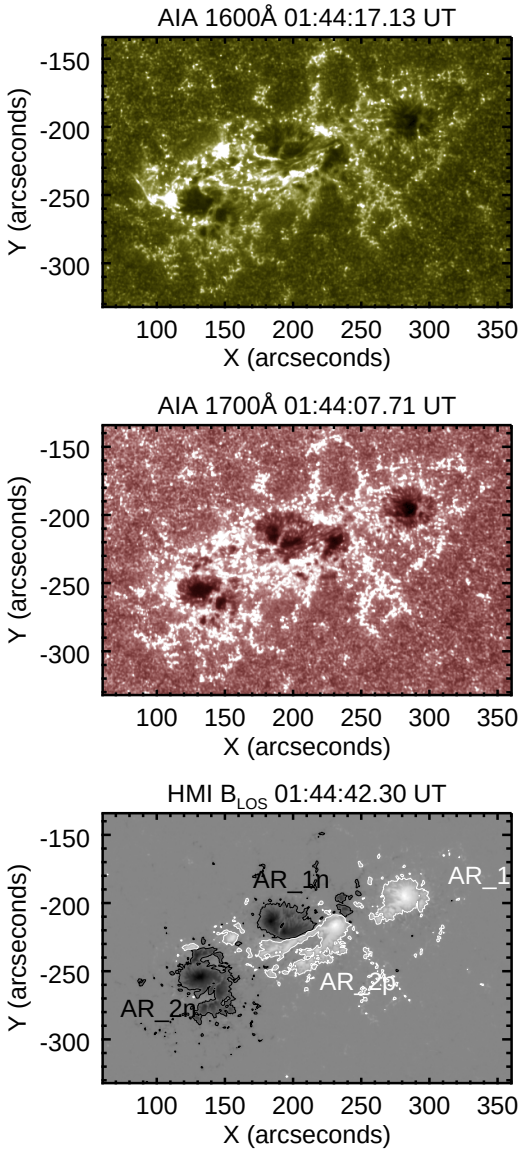

Fig. 2. Active region 11158 in AIA 1600Å (top), AIA 1700Å (middle), and HMI LOS magnetogram (bottom) on 2011-February-15. The white and black contours outline positive (+300 Gauss) and negative (-300 Gauss) polarities, respectively. The two sunspots in the northern pair are labeled AR_1p (leading sunspot) and AR_1n (trailing sunspot). The two sunspots in the southern pair are labeled AR_2p (leading sunspot) and AR_2n (trailing sunspot).

3. ANALYSIS

The technique used to calculate power maps as functions of space and time is similar to that employed by Jackiewicz & Balasubramaniam (2013) and further employed by Monsue et al. (2016). The general method is as follows: For a data set of N images, each power map $P(x, y, t_i)$ is generated by applying a Fourier transform to every pixel at (x, y) in the temporal direction, from t_i to $t_i + T$, where T is the length of the time segment. The power is averaged over a frequency band $\Delta\nu$ of user-defined width, centered on the frequency of interest. This process is repeated at every timestep, for starting times from t_0 to t_{N-N_T}.

The data set for AR 11158 consisted of $N = 749$ images (5 hours) of AIA observations in each channel. Each time segment T was set to 64 images (∼25.6 minutes). The value of T was chosen based on a balance between sufficient length to obtain frequencies close to that of the 3-minute period and not so long as to lose information on timescales over which the 3-minute power was previously observed to change. Each Fourier transform was applied without detrending the data since the frequency of interest was well outside the global flare signal. (As a check on this, a Fourier filter was applied with a cutoff period above 400 seconds. The power spectra for the periods of interest did not change.) If a saturated pixel was encountered in any segment t_i to $t_i + T$, it was excluded from the power map for that time segment, and the location (x, y) of that pixel was set to zero.

The frequency bandwidth $\Delta\nu$ was set to 1 mHz centered on $\nu \sim 5.6$ mHz . This is consistent with similar techniques applied in previous studies. For instance, Stangalini et al. (2011) used a 1-mHz frequency bandpass between 4.8 mHz (208.3 seconds) and 5.8 mHz (172.4 seconds) when calculating power maps around 5.6 mHz for the chromosphere and photosphere. Tripathy et al. (2018) also used a band of 1 mHz over 0.1-mHz steps from 1 to 10.5 mHz. Reznikova et al. (2012) used a bandpass of only 0.4 mHz. . .

With these input parameters, a frequency resolution $\partial\nu$ of ∼0.65 mHz was obtained. Two frequencies were obtained within $\Delta\nu$ at 5.21 mHz (192.00 seconds) and 5.86 mHz (170.67 seconds).

The average power over $\Delta\nu$ for each unsaturated pixel in time segment T from t_i to $t_i + T$ was taken to be the 3-minute power in each power map. Since only two frequencies were obtained within $\Delta\nu$, and were centered around the frequency of interest, the average was computed without the application of a filter.

Power maps representing the 3-minute power over NOAA AR 11158 in space and time were obtained at every starting point in the time series (up to $N - T$) by applying a Fourier transform to the signal from each pixel, and averaging the power within the 1-mHz frequency bandwidth $\Delta\nu$ centered around 5.6 mHz (3 minutes).

4. RESULTS AND DISCUSSION

The following section first discusses powermap results that were consistent throughout the time series, followed by before, during, and after the X-class flare.

Figures 3, 4, and 5 each show intensity images and corresponding spatial distibution of the 3-minute power in AIA 1600Å and AIA 1700Å before, during, and after the X-class flare, respectively. The contours overlaid on each image represent the HMI B_{LOS} magnetogram at ±300 Gauss, which corresponds closely with the boundary of the outer penumbra. This also helps to identify possible correlations between oscillatory power and magnetic field strength. Both the contour data and the intensity maps were obtained by averaging over the same time segment from which the power map was computed. (It should be noted that the alignment procedures may have resulted in a slight offset between the channels, in addition to any existing LOS affects.)

The particular time segments presented here were chosen based on the presence of interesting features in the power maps or distinct patterns in the light curve. Several key observations in the spatial distribution of 3-minute power were relatively consistent throughout the time series.

The power appears constrained to the immediate vicinity of the active region; there is very little enhancement beyond this (examination of the isolated power maps outside the active region confirmed that this was not merely a visual scaling effect).

The 3-minute power tends to be suppressed directly over the center of the umbra, with a ring-like pattern of enhanced power around the edges of the umbra, similar to results from Reznikova et al. (2012) for AIA UV emission.

Power enhancement occurs in relatively small regions. For example, in Figure 3, there is a distinct bright spot with high power along the lower edge of the penumbra boundary of AR_1p, with an area of $\sim 6" \times 6"$.

The concentration of power enhancement in small areas located in the vicinity of sunspot umbrae suggests that these small areas of the chromosphere are responding directly to the injection of energy by a beam of non-thermal particles.

Locations of enhanced power tended to have high intensity in the corresponding intensity image. However, enhanced power did not necessarily appear in every location of high intensity. This is most clearly visible in AIA 1600Å.

The regions of enhanced 3-minute power were usually located along the boundaries of magnetic field strength at ±300 Gauss, approximately over the outer penumbra boundary.

The location of these enhancements does not move across the AR. Rather, it remains in one place until it fades away. One of the most prominent locations of enhanced power occurs before the flare at the bottom of the leading sunspot in the northern pair. The change in location with time of both flare intensity and 3-minute power implies that the source of the beam of non-thermal particles changes as well.

4.1. *Pre-flare, 00:00-01:44 UT*

Although this time segment took place during the precursor phase of the X-class flare, it also took place *after* a C-class flare that occurred an hour before the X-flare, between 00:30 and 00:45 UT, as well as another event the day before on 10 February 2011. The emission from the C-flare originated from AR_2n.

Figure 3 shows pre-flare intensity images and corresponding power maps for the time segment immediately prior to the *GOES* start time. The "J-shaped" ribbon feature can be seen in the center of the intensity images and the power map along the left edge of the boundary of AR_1n, most visible in AIA 1600Å. The prominent region of enhanced power along the lower penumbral boundary of AR_1p emerged earlier and persisted until the decay phase of the X-flare. Interestingly, the C-flare occurred on the opposite side of AR 11158. Movies of the active region intensity leading up to the X-flare reveal intermittent appearances of high intensity here. Due to the length of T, the enhancement in power was consistently present in the power maps. any activity in this region. Future work will involve the investigation into the magnetic configuration of this region and potential connections between this spot and earlier events. Locations of enhanced power are, for the most part, located along umbra/penumbra boundaries, though a ribbon-like shape through the center of AR_1n is also observed.

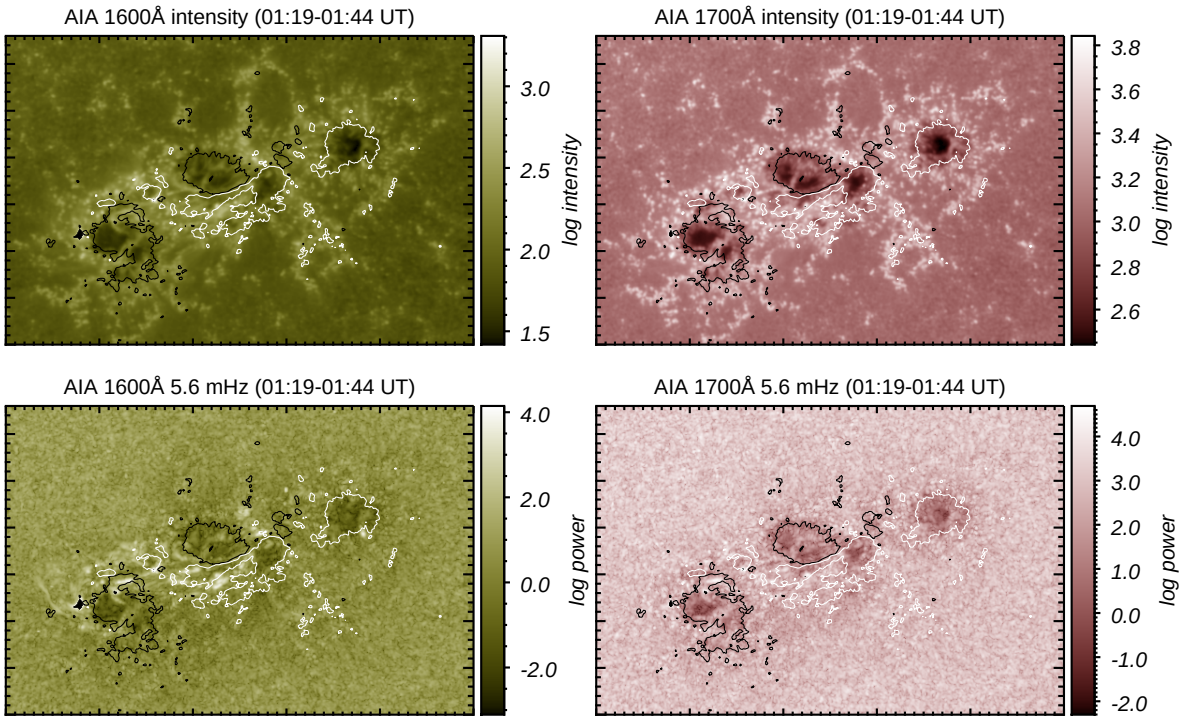

Fig. 3. Intensity and spatial distribution of 3-minute power immediately prior to the X-class flare between 01:19 and 01:44 UT on 15 February 2011, in log scale to bridge large contrasts. Locations whose time segment included saturated pixels were set to zero. Contours indicate the approximate position of HMI B_{LOS} at ±300 Gauss. White and black contours represent positive and negative polarities, respectively. The dimensions of each image are the same as labeled on the axes in Figure 2.

4.2. *During the flare, 01:44-02:30 UT*

Figure 4 shows intensity images and corresponding power maps for the time segment between 01:45 and 02:10 UT, just after the *GOES* start time (01:44 UT) until a few minutes after the *GOES* end time (02:06 UT). This covered the maximum amount of flare emission: from the start of the impulsive phase through as much of the decay phase as allowed by T. Pixels that saturated were excluded from the maps to improve contrast between the remaining pixels.

Due to the short timescales over which flare dynamics typically occur, the instrumental sampling rate here is too low to obtain sufficient time resolution. The sampling time $T \approx$25 minutes used here did not allow the isolation of any one flare phase as it was a few minutes longer than the entire duration between the official *GOES* start and end times. (about 22 minutes). While the choice of T was necessary to obtain sufficient frequency resolution, this does come at the expense of temporal resolution. The enhanced emission at the 3-minute period in integrated emission observed by Milligan et al. (2017) appeared to start around 01:44 and faded beyond the 99% confidence limit by ∼02:02, with slightly enhanced power beyond this until ∼02:10 in AIA 1700Å. These timescales over which the oscillatory power changed were much shorter than the sample time length used here.

Due to the large number of pixels that saturated during the flare, not much spatial information can be extracted from power maps obtained during the time that enhanced chromospheric emission was previously observed. peak flare emission, particularly from the AR center and parts of the outside sunspots, where emission reaches further into as the flare develops. According to the review from Inglis & Nakariakov (2009), QPPs in flare emission often don't last longer than three or four periods, so extracting these oscillations would be difficult even without saturation with the current methods.

It can be observed that the spot in AR_1p fades away in the power maps obtained from gradual phase only (no emission from precursor or impulsive phases contributing to power map).

For the current data set, the peak in AIA emission occurred around 01:53 UT (01:52:41.12 for 1600Å, and 01:52:55.71 for 1700Å), about 3 minutes before the *GOES* peak time (01:56 UT). Both UV light curves show a slight increase at the *GOES* end time (02:06), as well as a few other times during the decay phase.

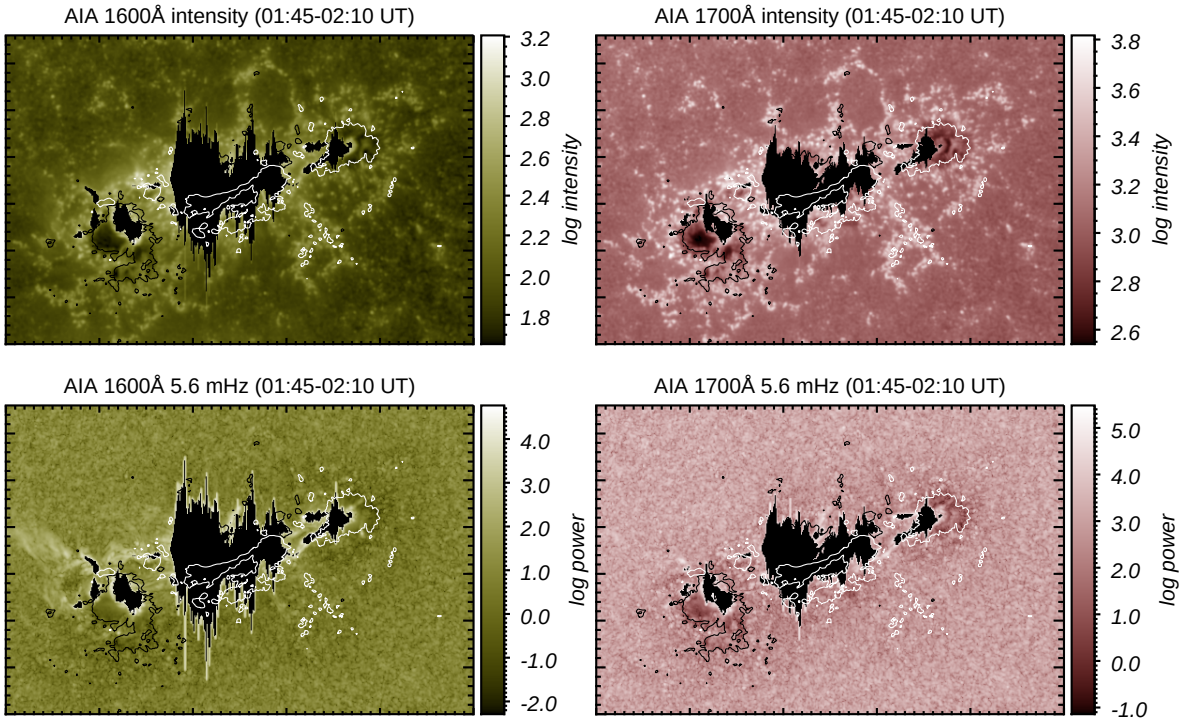

Fig. 4. Same as Figure 3, during the X-class flare between 01:45 and 02:10 UT on 15 February 2011.

4.3. *Post-flare, 02:30-05:00*

Figure 5 shows post-flare intensity images and corresponding power maps for the time segment between 03:00 and 03:25, well into the gradual phase of the x-flare. This time period includes the first of two small events that occurred after the X-class flare within the five-hour time series.

This particular time segment was chosen to present as the post-flare oscillatory power because of the presence of several distinct, small regions of enhancement in the center, right around AR_2p.

4.4. *Discrete wavelet analysis*

The technique described in §3 was applied to the integrated flux from AR 11158 at discrete intervals of T = 64 images with no overlap (i.e. for start time t_0, then $t_1 = t_0 + T$, etc.). This provided a "quick and dirty" way to compare the spectral power at a range of frequencies. This method produces similar results to those obtained with wavelet analysis, though at lower resulting frequency and time resolution. The results are are shown in Figure 6 for frequencies between 2.5 and 20.0 mHz (400 and 50 seconds, respectively). The central frequency $\nu_c = 5.56$ mHz and the frequency bandpass $\Delta\nu$ at 5 and 6 mHz are marked by the horizontal dashed lines. The power at all frequencies appears to be enhanced during the X-flare compared to their non-flaring power before and after. During the small events before and after the flare, the power at lower frequencies is enhanced, but the power at higher frequencies is suppressed relative to the same frequencies for adjacent time segments.

At all points in time when power enhancement occurs for any frequency, there appears to be a correlation with flux increase.

4.5. *Temporal evolution of 3-minute power*

The evolution of the 3-minute power with time was calculated from the power maps by summing over x and y in each map $P(x, y, t_i)$, and taking the total to be the 3-minute power of the active region during each time segment. This is shown in Figure 7. Each point is plotted as a function of the center of the time segment over which the Fourier transform was applied to obtain that point. The axis labelled $T = 64$ shows the scale for this length of time.

Power as a function of time obtained from total flux and power maps is shown to check for possible contradictions between the two. Integrating flux over the AR before applying the Fourier transform has the potential effect of reducing or canceling signal from pixels whose intensity variations are out of phase.

The reason for the apparent periodicity in the plots of 3-minute power with time is unclear. The calculations were repeated for power centered on the 5-minute period and the 2-minute period, and resulted in the same trend, with the additional observation that the length of the central period scaled with the period in the plot of power vs. time. This pattern is attributed to computational effects.

The persistence of the 3-minute power toward the end of the gradual phase in AIA 1700Å is consistent with the results of the wavelet analysis carried out by Milligan et al. (2017).

The small periodicities can be difficult to extract from the global lightcurve (Van Doorsselaere et al. 2016).

If the location of power enhancement does reveal sites of energy injection, then it remains possible that changes in energy source coincides with the location of power changes.

Almost all events before and after the main X-class flare occurred in AR_2n, including briefly at the beginning of the time series.

3-minute oscillations are interpreted as slow, propagating magnetoacoustic waves, which have a characteristic excitation mechanism and damping rate, depending on the local plasma conditions where they originate. The timescales over which the oscillatory power is expected to change depends on the nature of the oscillations themselves, or maybe the cooling rate of the plasma. The expected timescales would depend on the cooling rate of the plasma (images) and the damping time/mechanisms of the 3-minute oscillations.

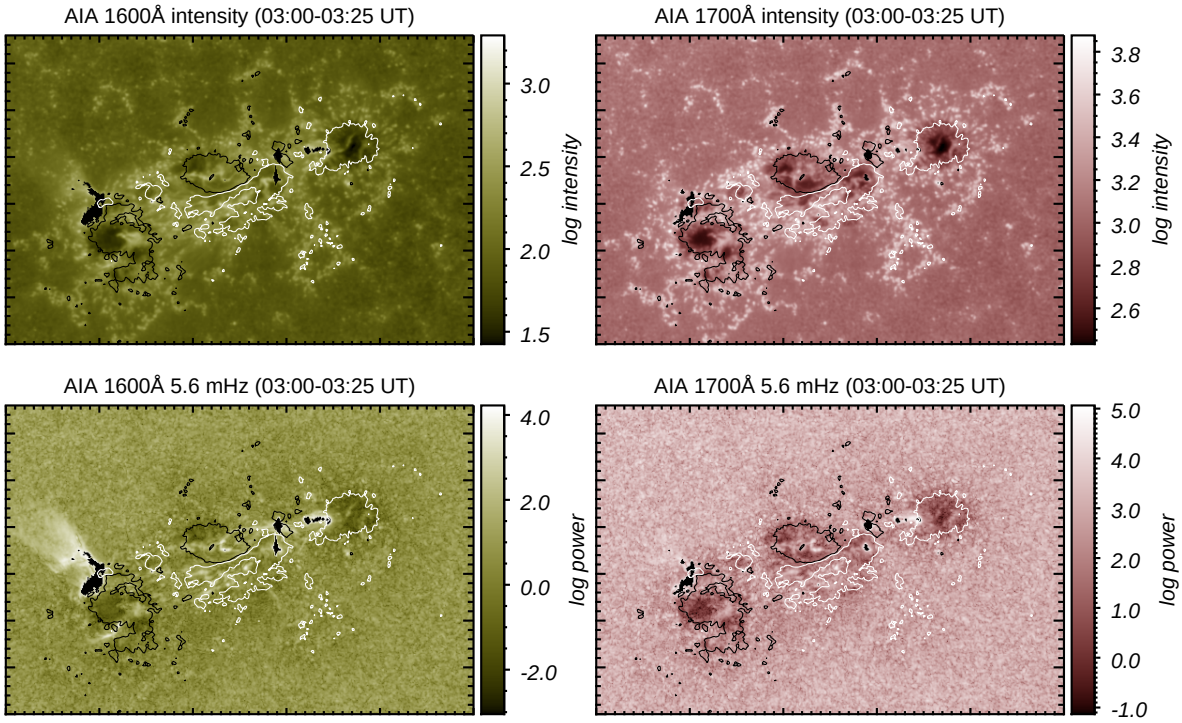

Fig. 5. Same as Figure 3, after the X-class flare between 03:00 and 03:25 UT on 15 February 2011.

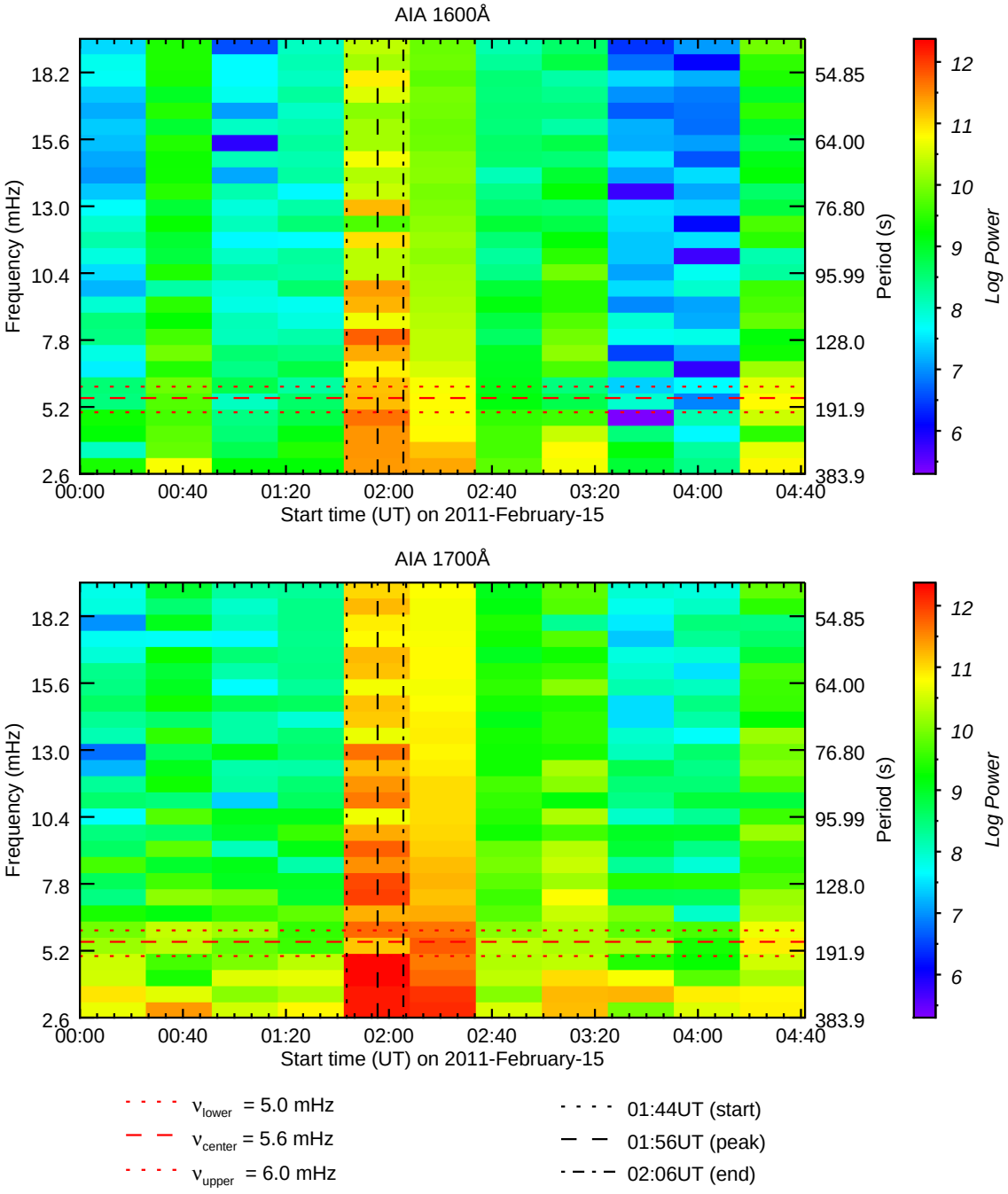

Fig. 6. Time-frequency power plots from AIA 1600Å (top panel) and AIA 1700Å (bottom panel), obtained by applying a Fourier transform to integrated emission from NOAA AR 11158 in discrete time increments of 64 frames (∼25.6 minutes) each. The dashed horizontal line marks the central frequency ν_c at ∼5.6 mHz, corresponding to a period of 3 minutes. The dotted horizontal lines on either side of ν_c mark the edges of the frequency bandpass $\Delta\nu = 1$ mHz. The vertical lines mark the flare, start, peak, and end times as determined by *GOES*. The power is scaled logarithmically and over the same range in both channels.

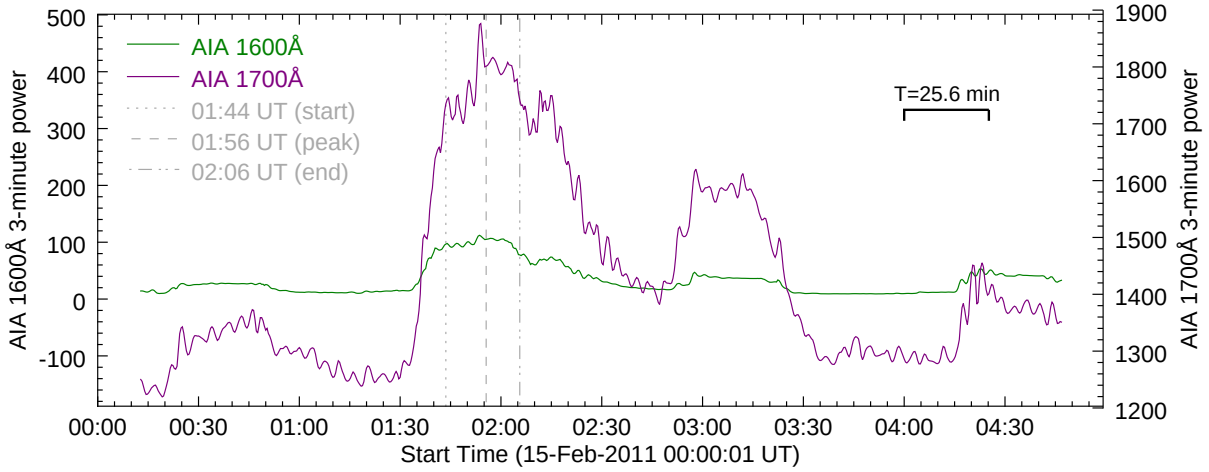

Fig. 7. Temporal evolution of the 3-minute power $P(t)$ in AIA 1600Å (green curve) and AIA 1700Å (purple curve). $P(t)$ per unsaturated pixel, obtained by summing over power maps whose pixel values = 0 if saturated, then divided by number of unsaturated pixels. Each point in time is plotted as a function of the center of the time segment over which the Fourier transform was applied to obtain the power map over which the point was summed. The vertical dashed lines mark the *GOES* start, peak, and end times of the flare at 01:44, 01:56, and 02:06 UT, respectively.

5. CONCLUSIONS

In this work, we have presented spatial distribution of the 3-minute oscillations associated with the X-class flare that occurred in AR11158 on 15 February 2011. Key points are as follows:

1. Small, distinct regions of enhanced power show that the chromospheric plasma does not oscillate as one body.
2. Location relative to AR same as enhanced intensity associated with the flare, which supports the theory of oscillation in response to energy injection via accelerated non-thermal particles.
3. Variation in enhancement location throughout flare phases indicates a possible change in source of energy input.

Future work will involve smaller flares to avoid saturation issues. It is possible that important spatial information is contained in location of the flare core, but cannot be extracted due to the saturation in the pixels. Saturation does not occur as often for flares of less powerful classes. Since several of the data images saturated during the main phase of the flare, spatial information cannot be obtained at the core location of the flare. It may be worthwhile to apply these methods to a less powerful flare.

The temporal behavior of oscillations during the main flare remains inconclusive due to the necessary balance between temporal and frequency resolution. Techniques to improve temporal resolution, such as the standard wavelet analysis presented by Torrence & Compo (1998), will allow study of chromospheric behavior on timescales comparable to those over which flare dyanmics are known to occur.

The pre-flare data shown in this work may not be the best representation since another, smaller flare took place in the middle of it. It may be worthwhile to obtain more data at earlier times

Acknowledgements: ?

REFERENCES

Awasthi, A. K., Rudawy, P., Falewicz, R., Berlicki, A., & Liu, R. 2018, ApJ, 858, 98, doi: 10.3847/1538-4357/aabd76

Brosius, J. W., & Daw, A. N. 2015, ApJ, 810, 45, doi: 10.1088/0004-637X/810/1/45

Chae, J., & Goode, P. R. 2015, ApJ, 808, 118, doi: 10.1088/0004-637X/808/2/118

De Pontieu, B., Title, A. M., Lemen, J. R., et al. 2014, SoPh, 289, 2733, doi: 10.1007/s11207-014-0485-y

Fletcher, L., Hannah, I. G., Hudson, H. S., & Innes, D. E. 2013, ApJ, 771, 104, doi: 10.1088/0004-637X/771/2/104

Inglis, A. R., Ireland, J., & Dominique, M. 2015, ApJ, 798, 108, doi: 10.1088/0004-637X/798/2/108

Inglis, A. R., & Nakariakov, V. M. 2009, A&A, 493, 259, doi: 10.1051/0004-6361:200810473

Jackiewicz, J., & Balasubramaniam, K. S. 2013, ApJ, 765, 15, doi: 10.1088/0004-637X/765/1/15

Kumar, B., & Ravindra, B. 2006, Journal of Astrophysics and Astronomy, 27, 425, doi: 10.1007/BF02709368

Kwak, H., Chae, J., Song, D., et al. 2016, ApJL, 821, L30, doi: 10.3847/2041-8205/821/2/L30

Lemen, J. R., Title, A. M., Akin, D. J., et al. 2012, SoPh, 275, 17, doi: 10.1007/s11207-011-9776-8

McAteer, R. T. J., Gallagher, P. T., Bloomfield, D. S., et al. 2004, ApJ, 602, 436, doi: 10.1086/380835

McAteer, R. T. J., Gallagher, P. T., Williams, D. R., et al. 2003, ApJ, 587, 806, doi: 10.1086/368304

Milligan, R. O., Fleck, B., Ireland, J., Fletcher, L., & Dennis, B. R. 2017, ApJL, 848, L8, doi: 10.3847/2041-8213/aa8f3a

Monsue, T., Hill, F., & Stassun, K. G. 2016, AJ, 152, 81, doi: 10.3847/0004-6256/152/4/81

Pesnell, W. D., Thompson, B. J., & Chamberlin, P. C. 2012, SoPh, 275, 3, doi: 10.1007/s11207-011-9841-3

Reznikova, V. E., Shibasaki, K., Sych, R. A., & Nakariakov, V. M. 2012, ApJ, 746, 119, doi: 10.1088/0004-637X/746/2/119

Scherrer, P. H., Schou, J., Bush, R. I., et al. 2012, SoPh, 275, 207, doi: 10.1007/s11207-011-9834-2

Schou, J., Scherrer, P. H., Bush, R. I., et al. 2012, SoPh, 275, 229, doi: 10.1007/s11207-011-9842-2

Stangalini, M., Del Moro, D., Berrilli, F., & Jefferies, S. M. 2011, A&A, 534, A65, doi: 10.1051/0004-6361/201117356

Sutmann, G., Musielak, Z. E., & Ulmschneider, P. 1998, A&A, 340, 556

Sutmann, G., & Ulmschneider, P. 1995a, A&A, 294, 232

—. 1995b, A&A, 294, 241

Sych, R., Nakariakov, V. M., Karlicky, M., & Anfinogentov, S. 2009, A&A, 505, 791, doi: 10.1051/0004-6361/200912132

Torrence, C., & Compo, G. P. 1998, Bulletin of the American Meteorological Society, 79, 61

Tripathy, S. C., Jain, K., Kholikov, S., et al. 2018, Advances in Space Research, 61, 691, doi: 10.1016/j.asr.2017.10.033

Van Doorsselaere, T., Kupriyanova, E. G., & Yuan, D. 2016, SoPh, 291, 3143, doi: 10.1007/s11207-016-0977-z

Viereck, R., Hanser, F., Wise, J., et al. 2007, in Proc. SPIE, Vol. 6689, Solar Physics and Space Weather Instrumentation II, 66890K